Electric field effects in STM imaging

Kurt Stokbro, Ulrich Quaade and Francois Grey
Mikroelektronik Centret, Danmarks Tekniske Universitet, Bygning 345ø, DK-2800 Lyngby, Denmark.
(February 7, 2008)

We present a high voltage extension of the Tersoff-Hamann theory of STM images, which includes the effect of the electric field between the tip and the sample. The theoretical model is based on first principles electronic structure calculations and has no adjustable parameters. We use the method to calculate theoretical STM images of the monohydrate Si(100)-H(2×1) surface with missing hydrogen defects at −2 V and find an enhanced corrugation due to the electric field, in good agreement with experimental images.

I. INTRODUCTION

First principles electronic structure calculations have become an important tool in interpreting STM experiments. Calculations of theoretical STM images are often based on the theory by Tersoff and Hamann [1], which states that the the STM current is proportional to the local density of states(LDOS) of the sample. In this theory it is assumed that the potential is flat between the tip and the sample, and the vacuum level given by the sample work function. However, for relatively high biases ($>$ 2 V), which are often used in STM experiments on semiconductor surfaces, the electric field strength in the tunnel region can be relatively high and must be included in the theoretical model [2].

In this paper we extend the Tersoff-Hamann formalism to include the electric field in the tunnel region, and apply the theory to calculate the corrugation of a single missing hydrogen defect on the monohydride Si(100)-H(2×1) surface. We find that the corrugation is strongly increased by the electric field, mainly due to polarization effects and partly due to changes in the tunnel barrier.

The organization of the paper is the following: In section II we present the basic theory for calculating field dependent STM images, and in section III we show how the electric field effect can be included in the first principles calculation. In section IV we apply the formalism to calculate the corrugation of a missing hydrogen defect on the monohydrate Si(100)-H(2×1) surface and in section V we conclude.

II. THEORY

In this section we present the basic theory for calculating field dependent STM images. The derivation will follow Chen [3] closely. Figure 1 shows the tunnel junction between the tip and sample. Using the modified Bardeen approach [3], the tunnel current is given by

$$I = \frac{2\pi e}{\hbar}\sum_{\mu\nu}[f(\epsilon_\nu - eV_{\rm b}) - f(\epsilon_\mu)]|M_{\mu\nu}|^2\delta(\epsilon_\mu - \epsilon_\nu), \quad (1)$$

$$M_{\mu\nu} = \frac{\hbar^2}{2m}\int_\Sigma d\vec{S}\cdot(\chi_\nu^*\vec{\nabla}\psi_\mu - \psi_\mu\vec{\nabla}\chi_\nu^*), \quad (2)$$

where the integral in Eq. (2) is over any separating surface Σ lying entirely within the vacuum region separating the two sides. The sample bias, $V_{\rm b}$ defines the difference between tip and sample Fermi levels, and $f(\epsilon)$ is the Fermi function. The modified sample(tip) wave functions ψ_μ (χ_ν) are solutions to the Schrödinger equation with modified sample(tip) potential U_s (U_t). These potentials are given by the tunnel potential U upto the separating surface, Σ, and are equal to the vacuum level beyond the separating surface, thus $U = U_s + U_t$ and $U_sU_t = 0$. The gradient of U in the tunnel region determines the tip induced electric field, $\mathbf{E} = \nabla U/e$.

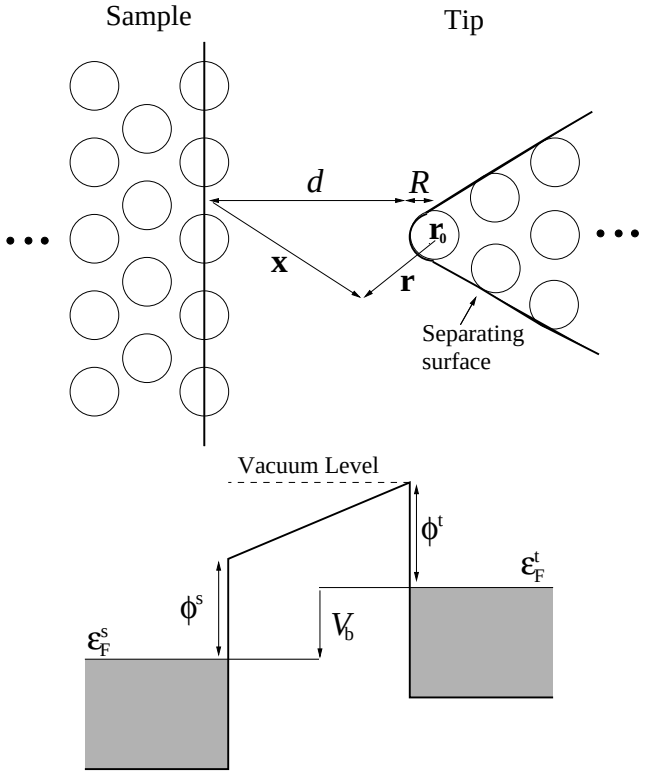

FIG. 1. The STM tunnel region and tunnel potential.

We assume that the tip is grounded and the vacuum level determined by the tip workfunction. Furthermore, we assume that the tunnel current is due to a single atom

at the tip apex. We place the separating surface, Σ, just outside the atomic radius, R, of this atom (see Fig. 1). The position of the tip we denote by $\mathbf{r}_0$, and the tip sample distance is given by $d = r_0 - R$. Since the tip potential equals the vacuum level beyond the separating surface, it is straightforward to expand the modified tip wave functions in real spherical harmonics, Y_l^m, and obtain

$$\chi_\nu(\mathbf{r}) = \sum_{lm} C_{lm}^\nu k_l(\kappa_\epsilon r)/k_l(\kappa_\epsilon R) Y_l^m(\hat{r}), \quad (3)$$

$$C_{lm}^\nu = \int_{4\pi} \chi_\nu(R\hat{r}) Y_l^m(\hat{r}) d\hat{r}, \quad (4)$$

$$\kappa_\epsilon = \sqrt{2m(\phi^t + eV_\mathrm{b} + \epsilon_F^s - \epsilon)}/\hbar, \quad (5)$$

where $\mathbf{r}$ is the distance from the tip atom, k_l the spherical modified Bessel functions, κ_ϵ the inverse decay length of the electron states in vacuum, and ϵ_F^s the Fermi level of the sample. Following Ref [3] we observe that the tip Green's function, defined by $(-\hbar^2\nabla^2/2m + U_t)G(\mathbf{r}) = 4\pi\delta(\mathbf{r})$, is related to the tip wave-function by $k_l(\kappa_\epsilon r)Y_l^m(\hat{r}) = \kappa_\epsilon^{-l-1} a_l \hat{A}_{lm} G(\mathbf{r})$, where the differential operators $\hat{A}_{lm}$ are defined in Table 1, and the coefficients a_l defined by $a_{\{s,p,d\}} = \{\sqrt{1/4\pi}, \sqrt{3/4\pi}, \sqrt{15/16\pi}\}$. We now obtain the current

$$I = 8\pi^3 \frac{\hbar^3 e}{m^2} \int_{\epsilon_F^s}^{\epsilon_F^s + eV_\mathrm{b}} \sum_{lm,\mu} \left| \frac{a_l \hat{A}_{lm} \psi_\mu(\mathbf{r_0})}{\kappa_\epsilon^{l+1} k_l(\kappa_\epsilon R)} \right|^2 \delta(\epsilon - \epsilon_\mu) \times D_{lm}(\epsilon - eV_\mathrm{b}) d\epsilon, \quad (6)$$

where we have neglected coherence between partial tip states and $D_{lm}(\epsilon) = \sum_\nu |C_{lm}^\nu|^2 \delta(\epsilon - \epsilon_\nu)$ are partial tip density of states per unit volume.

We have calculated D_{lm} for a single W atom on a W(110) surface using $R = 3$ bohr. We find that it is nearly independent of m, and average l dependent values are $D_{\{s,p,d\}}(\epsilon) \approx \{0.002\Theta_{[-10,20]}(\epsilon),\ 0.002\Theta_{[0,20]}(\epsilon),\ 0.002\Theta_{[-4.5,3.5]}(\epsilon)\}$ eV^{-1}bohr^{-3}, where the step function, $\Theta_{[a,b]}(x)$, is one for x in the interval $a < x < b$ and zero otherwise. Using these values we obtain the current

$$I = \int_{\epsilon_F^s}^{\epsilon_F^s + eV_\mathrm{b}} e^{2\kappa_\epsilon R} \sum_{lm} B_{lm}(\epsilon - eV_\mathrm{b}) \rho_{lm}(d + R, \epsilon) d\epsilon, \quad (7)$$

where distances are in bohr, energies in eV and current in Amperes. Parameters B_{lm} are defined in Table 1. The main quantity is the sample LDOS, $\rho_{lm}(\mathbf{x}, \epsilon) = \sum_\mu |\hat{A}_{lm}\psi_\mu(\mathbf{x})|^2 \delta(\epsilon - \epsilon_\mu)$. The wave functions ψ_μ are calculated in the external electric field from the tip, and we approximate this field by a planar electric field of strength E. For a given tip-sample distance d, the field strength is determined from the equation

$$U_s(d, E) = \phi^t + eV_\mathrm{b} + \epsilon_F^s, \quad (8)$$

where U_s is the effective sample potential in planar field E. This equation assumes that the tip behaves as a metallic sphere of radius R, consistent with the spherical potential-well model of the tip used in Eq. (3) [1].

The main result of this paper, Eq. (7), is a high voltage generalization of the Tersoff-Hamann expression [1] for the STM current. The main differences between Eq. (7) and the expression by Tersoff and Hamann are the integration over the electronic states and the calculation of the sample wave functions in an external electric field. We also include higher angular tip states [3], whereas the Tersoff-Hamann formulation is for an s-type state only. For the systems we have investigated we find that $m > 0$ terms are more than one order of magnitude smaller than $m = 0$ terms and can therefore be neglected. Of the $m = 0$ states, we find that the $l = 0$ state gives a contribution which is twice that of $l > 0$ states. In the following we will only consider the $l = 0$ contribution, since we have found that this contribution best describes the experimental images we consider. However, we note that occasionally we see a change in the image contrast, which might be due to dominance of $l > 0$ states for special tip geometries.

l	m	$B_{lm}(\epsilon)$	$\hat{A}_{lm}$
0	0	$0.007R^2\Theta_{[-10,20]}(\epsilon)$	1
1	-1	$0.02R^4(1+\kappa_\epsilon R)^{-2}\Theta_{[0,20]}(\epsilon)$	$\frac{\partial}{\partial x}$
1	0	$0.02R^4(1+\kappa_\epsilon R)^{-2}\Theta_{[0,20]}(\epsilon)$	$\frac{\partial}{\partial z}$
1	1	$0.02R^4(1+\kappa_\epsilon R)^{-2}\Theta_{[0,20]}(\epsilon)$	$\frac{\partial}{\partial y}$
2	-2	$0.03R^6(3+3\kappa_\epsilon R+\kappa_\epsilon^2R^2)^{-2}\Theta_{[-4.5,3.5]}(\epsilon)$	$\frac{\partial^2}{\partial x \partial y}$
2	-1	$0.03R^6(3+3\kappa_\epsilon R+\kappa_\epsilon^2R^2)^{-2}\Theta_{[-4.5,3.5]}(\epsilon)$	$\frac{\partial^2}{\partial y \partial z}$
2	0	$0.03R^6(3+3\kappa_\epsilon R+\kappa_\epsilon^2R^2)^{-2}\Theta_{[-4.5,3.5]}(\epsilon)$	$\frac{\sqrt{3}\partial^2}{\partial z^2} - \frac{\kappa_\epsilon^2}{\sqrt{3}}$
2	1	$0.03R^6(3+3\kappa_\epsilon R+\kappa_\epsilon^2R^2)^{-2}\Theta_{[-4.5,3.5]}(\epsilon)$	$\frac{\partial^2}{\partial x \partial z}$
2	2	$0.03R^6(3+3\kappa_\epsilon R+\kappa_\epsilon^2R^2)^{-2}\Theta_{[-4.5,3.5]}(\epsilon)$	$\frac{\partial^2}{\partial x^2} - \frac{\partial^2}{\partial y^2}$

TABLE I. Definition of the parameters B_{lm} and differential operators $\hat{A}_{lm}$ used in Eq. (7). The step function, $\Theta_{[a,b]}(x)$, is one for x in the interval $a < x < b$ and zero otherwise.

III. CALCULATION OF SURFACE ELECTRONIC STRUCTURE IN FIELD E

The electronic structure calculations are based on density functional theory [4,5] using the Generalized Gradient Approximation of Ref. [6] for the exchange-correlation energy. Ultra-soft pseudo potentials [7] including the nonlinear core correction [8] are used to describe hydrogen and silicon and the wave functions are represented in a plane-wave basis set with kinetic energy cutoff 20 Ry. At distances larger than 4 Å from the surface, the wave functions are obtained by outward integration using the average effective potential perpendicular to the slab [9].

In the following we will consider the monohydrate Si(100)-H(2×1) surface, which we model by a (2×1) slab with 12 layers of silicon atoms, and a vacuum region of 10 Å. We apply an external electric field to the surface, by inserting a dipole layer in the middle of the vacuum region [10]. The effect of mobile carriers is introduced by fixing the atoms on the the back surface of the slab in their bulk positions [11]. This gives rise to half-filled surface states in the middle of the band gap, and this surface is therefore metallic. Depending on the direction of the external field the surface states accept or donate electrons. To obtain the field dependence of the wave functions we calculate the wave functions for two fields, E_1, E_2 , which bound the field range in the experiment. The wave functions at a given field, $E_1 < E < E_2$, are then obtained by logarithmic interpolation between the wave functions at E_1 and E_2.

Figure 2 shows the effective one-electron potentials for calculations with external fields of $E = 0.6$ V/Å and $E = -0.8$ V/Å. While the potential on the back surface is the same for both fields, the potential on the monohydrate(front) surface bends upwards for positive fields and downwards for negative fields, respectively.

The inset in Fig. 2 shows the band bending in the slab calculation compared with the band bending in a n-type sample with $N_D = 10^{18}$ cm^{-3}. The band bending calculation is based on standard band bending theory with non-degenerate statistics. [12] For the n-type sample the Fermi level is close to the conduction band, and we have the well known depletion and inversion for positive fields. In the case of the slab calculation, mobile carriers are simulated by the half-filled dangling-bond states on the back surface, and since these states fix the Fermi level in the middle of the band gap, the band bending is nearly symmetric in the field. The experimental Fermi level is given by [13]

$$\epsilon_F^s = \epsilon_g/2 - 0.49kT + kT\log(\frac{N_D}{n_i}), \tag{9}$$

$$\epsilon_g = 1.17 - \frac{4.73\times10^{-4}T^2}{T+636}\text{eV}, \tag{10}$$

$$n_i = 10^{16}T^{\frac{3}{2}}e^{\epsilon_g/2kT}\text{cm}^{-3}, \tag{11}$$

where ϵ_g is the bandgap, n_i the number of intrinsic carriers and T the surface temperature.

To correct for the difference in Fermi-level and band bending, Φ, between the experiment and the slab model we shift the STM voltage in the slab model by $\Delta V_{\rm b}^{+} = \tilde{\Phi} + \tilde{\epsilon}_g - \tilde{\epsilon}_F^s - (\Phi + \epsilon_g - \epsilon_F^s)$ at positive bias, and $\Delta V_{\rm b}^{-} = \tilde{\Phi} - \tilde{\epsilon}_F^s - (\Phi - \epsilon_F^s)$ at negative bias (values with tilde are slab quantities). In this way we obtain that the energy window of electronic states which contributes to the current is the same in the slab model as in the experiment.

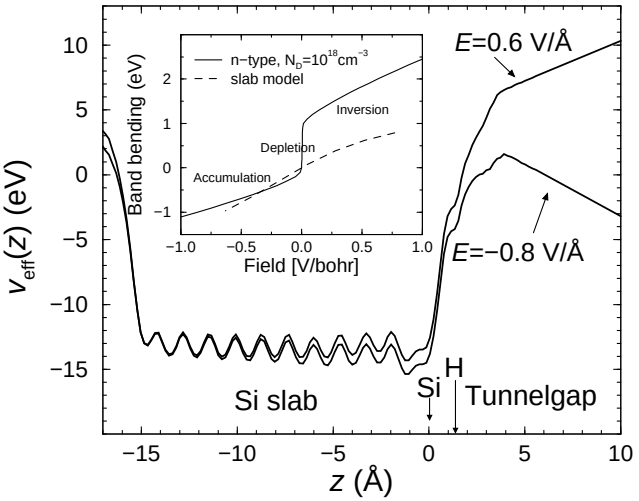

FIG. 2. The solid lines show the average effective potential, $v_{\rm eff}$, along the z axis(perpendicular to the slab) for external fields of 0.6 V/Å and -0.80 V/Å. The zero of the z axis is taken at the position of the first layer Si atoms, and the Fermi level defines the zero effective potential. The inset shows the band bending in the slab calculation(dashed line) compared with the band bending of a n-type sample with $N_D = 10^{18}$ cm^{-3} at room temperature(solid line) [12].

IV. THE STM CORRUGATION OF SI(100)-H(2×1)

In Fig. 3 we show a typical STM filled state image of the monohydrate Si(100)-H(2×1) surface. The bright vertical stripes originate from the hydrogen passivated silicon dimer rows, and the white spot originates from a silicon dangling bond due to a single missing hydrogen defect. Below the image we show the corrugation across the defect(solid line), compared with the simulated STM image of an s-state tip including field effects(dashed line) and without field effects(dotted line). In the range -5 Å$< x <$10 Å the theoretical curves were obtained using a c(4×4) cell with a single missing hydrogen defect, and outside this range using a (2×1) cell. We see that the corrugation of the defect is well described in the field dependent calculation, while it is less than half the value when the field is not included. The larger corrugation of the defect in the field dependent calculation is mainly due to polarization of the dangling bond. Away from the

defect the corrugation in both calculations is less than in the experiment. Calculations using p- or d-state tips do not give better agreement, and we suggest that the larger experimental corrugation away from the defect might be due to thermal vibrations on the surface.

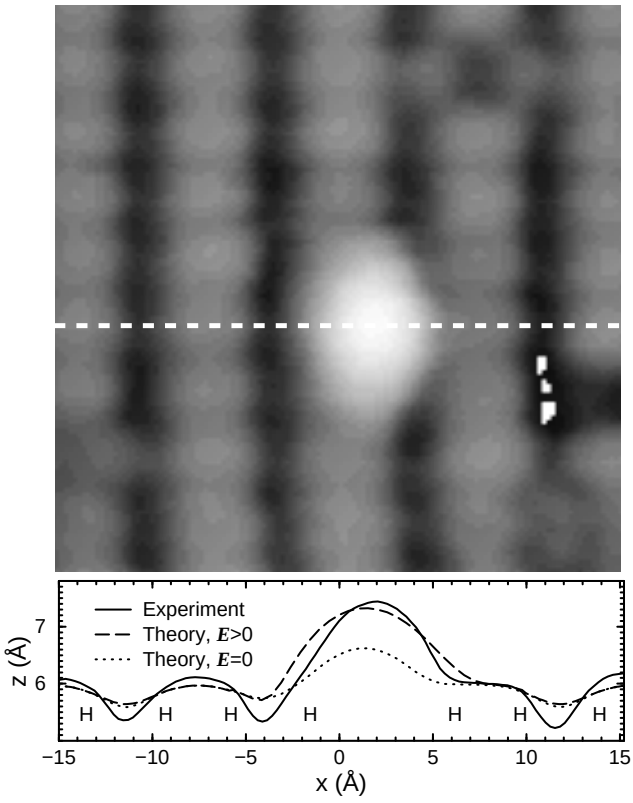

FIG. 3. Filled state STM image of a single hydrogen defect on the Si(100)-H(2×1) surface, recorded with $V = -1.6$ V and $I = 1$ nA. The plot shows the corrugation across the defect(solid line), together with the theoretical corrugation including electric field effects(dashed line) and without field effects(dotted line).

V. CONCLUSIONS

We have presented a high voltage extension of the Tersoff-Hamann model of STM images, which includes the electric field between tip and sample. We have applied the model to describe the corrugation of a single missing hydrogen defect, and find good agreement with experiment when field effects are included. At low voltages $|V_\mathrm{b}| < 3$ V, the field induced change of the corrugation is mainly due to polarization. For higher voltages $|V_\mathrm{b}| > 3$ V, as used in many atom manipulation experiments, the field also has a pronounced effect on the tunnel barrier, and we hope that the present work may prove useful for the analysis of such experiments.

[1] J. Tersoff and D. R. Hamann, Phys. Rev. B **31**, 805 (1985).
[2] H. Ness, A. J. Fisher, and G. A. D. Briggs, Surf. Sci. **380**, L479 (1997).
[3] C. J. Chen, *Introduction to Scanning Tunneling Microscopy* (Oxford University Press, New York, 1993).
[4] P. Hohenberg and W. Kohn, Phys. Rev. **136**, B864 (1964).
[5] W. Kohn and L. J. Sham, Phys. Rev. **140**, A1133 (1965).
[6] J. P. Perdew *et al.*, Phys. Rev. B **46**, 6671 (1992).
[7] D. Vanderbilt, Phys. Rev. B **41**, 7892 (1990).
[8] S. G. Louie, S. Froyen, and M. L. Cohen, Phys. Rev. B **44**, 8503 (1991).
[9] J. Tersoff, Phys. Rev. B **40**, 11990 (1989).
[10] J. Neugebauer and M. Scheffler, Phys. Rev. B **46**, 16067 (1992).
[11] P. Kratzer, B. Hammer, F. Grey, and J. K. Nørskov, Surf. Rev. Lett. **3**, 1227 (1996).
[12] R. Seiwatz and M. Green, J. Appl. Phys. **29**, 1034 (1958).
[13] S. M. Sze, *Semiconductor Devices* (Wiley, New York, 1985).